Pergamon

INDENTATION STRESS–STRAIN CURVES FOR "QUASI-DUCTILE" CERAMICS

A. C. FISCHER-CRIPPS† and B. R. LAWN

Materials Science and Engineering Laboratory, National Institute of Standards and Technology,
Gaithersburg, MD 20899, U.S.A.

Abstract—A micromechanical model describing "quasi-ductile" Hertzian contacts in otherwise brittle ceramics is developed. The elemental basis of the model is a discrete "fault" along an internal weak interface, constrained at its ends by an elastic matrix and subject to frictional sliding, in the subsurface zone of high shear stress in the Hertzian field. By summation over a prescribed density of shear faults within the active plastic zone, the analysis leads to a constitutive indentation stress–strain function, with special provision for the incorporation of microstructural variables. Experimental data from a series of mica-containing glass-ceramics with contiguous platelet microstructures are used to confirm the essential predictions of the model. It is demonstrated that plasticity increases with volume fraction and aspect ratio, but not size, of the platelets. Parametric evaluations by curve fitting the indentation stress–strain data allow for predictions of intrinsic stress–strain responses for the glass-ceramics in conventional uniform stressing states.

1. INTRODUCTION

The quest for plasticity has remained a persistent theme in the development of structural ceramics. The sensitivity of most ionic–covalent materials at room temperature to abrupt brittle failure [1] is so pervasive that even limited plasticity rarely occurs in ordinary stress–strain tests, even in compression, except in extremely coarse materials like rocks [2], composites and concretes [3]. It is only under conditions of extreme hydrostatic pressure, such as produced naturally in subterranean rock formations [2] and artificially in the confining belt apparatus used by geophysicists [4], that tensile fracture is suppressed and irreversible deformation states become evident in the stress–strain response. In that it relates to an underlying deformation mechanism other than dislocation motion, this irreversible deformation is referred to as "quasi-ductility" in the rock and concrete literature [3].

Recent studies using Hertzian indentation with spherical indenters have demonstrated that plasticity is attainable in ceramics with certain heterogeneous microstructures [5–10]. This plasticity registers as a deviation from linear elasticity on an "indentation stress–strain curve", i.e. a plot of contact pressure against relative contact/sphere radius [11–13]. Ordin-

arily, brittle ceramics show classical tensile macro-fractures, so-called Hertzian cone cracks [14–18], with only minor perturbation on the elastic response. However, in microstructures with constrained weak internal boundaries, coarse grains and high internal stresses, one observes a "plastic" damage zone in the subsurface compression-shear field, reminiscent of metals [11, 19]. These same heterogeneous ceramic microstructures are of interest for enhanced long-crack toughness, by grain-interlock bridging at the crack interface [20–23]. At the micromechanical level, the contact plastic zone is made up of an array of discrete, closed "shear faults" at the weak boundaries, with friction-resisted interfacial sliding [24, 25]. The internal friction is an important element in contact fatigue, because of attrition of the sliding interface in cyclic loading [25–27]. Apart from its insight into intrinsic deformation processes in ceramics, Hertzian contact is of great practical relevance to applications such as bearing performance, impact damage and biomechanical (e.g. dental) implants [28].

Contact plasticity is most apparent in second-phase platelet microstructures with high volume fractions, aspect ratios and weak interphase boundaries [8, 9, 25]. An extreme case is that in which the platelet volume fraction is sufficiently high as to form a contiguous second-phase network. This special microstructural type has figured prominently in the development of machinable ceramics, notably glass-ceramics [29–31], where interconnectivity enables easy material removal at the microscale yet preserves respectable long-crack toughness [32, 33]. These are

---

†Guest Scientist from the Department of Materials Science and Engineering, Lehigh University, Bethlehem, PA 18015, U.S.A.

also ideal microstructures in the context of the present study, in that the plasticity is almost exclusively from fault sliding—interconnectivity of the platelet phase avoids the complication of extensile cracking from the fault ends [34–36] that is characteristic of other quasi-ductile materials [5, 7, 10]. We will pay particular attention to this class of material in the interest of a case study, but emphasize the generality of our conclusions to any material system in which fault deformation dominates any accompanying extensile cracking.

Here we develop a model for the Hertzian stress–strain response for ceramics with discrete weak interfaces, with emphasis on the plastic component. Our model derives explicitly from the micromechanics of an elemental shear fault within the Hertzian field. We use experimental data from a series of machinable mica-containing glass-ceramics with contiguous platelet microstructures to confirm some of the important predictions of the modelling. The model enables us to derive an indentation stress–strain curve from a constitutive starting relation for individual shear faults in terms of extrinsic Hertzian stresses and intrinsic frictional resistance stresses. In this way, accessible microstructural parameters can be incorporated into the stress–strain function. Thus we show that plasticity increases with volume fraction and aspect ratio, but not size, of the constituent platelets. We also obtain evaluations for our specific glass-ceramic. We contend that the indentation curve is a reflection of the true stress–strain response

of the material in conventional uniform stressing states.

2. CASE STUDY ON GLASS-CERAMIC SYSTEM

2.1. Material characterization

For our material system we use a machinable glass-ceramic derived from a commercially available product from Corning Inc. (Corning, NY). Specimens were supplied to us in the form of a custom-made series of glass-ceramics, plus the base glass. The base glass is formed from the quaternary system K_2O–MgF_2–MgO–SiO_2, and the ensuing microstructure after a 4 h heat treatment has a near-contiguous fluorine tetrasilicic mica platelet network [37]. Modifications to the microstructure are readily effected by adjusting the heat treatment temperature: 1000, 1040, 1060, 1080 and 1120 C in our series of glass-ceramics.

The microstructure of the glass-ceramics is typified by the scanning electron micrograph in Fig. 1. Surface etching with dilute hydrofluoric acid reveals the mica platelets in the residual glass matrix. Digital image analysis of such micrographs indicates that the volume fraction of platelets remains effectively invariant over the range of heat treatment temperatures studied, but that the length and aspect ratio increases monotonically with continuing heat treatment. These variations are plotted in Fig. 2.

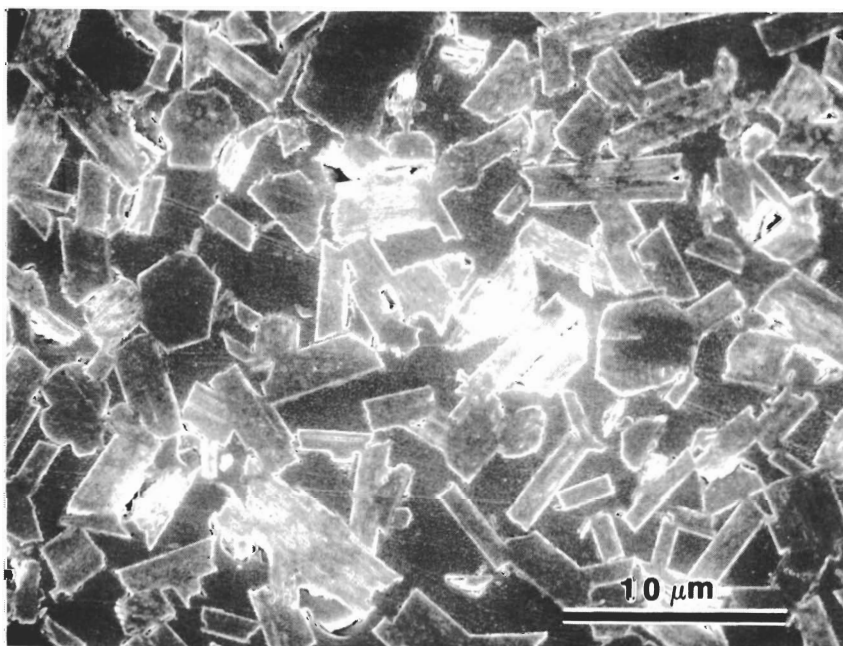Young's modulus measurements using an acoustic technique yield 70 ± 1 GPa for all materials in the series.

Fig. 1. Scanning electron micrograph of glass-ceramic heat-treated at 1120 C, surface-etched to reveal mica platelets in glass matrix.
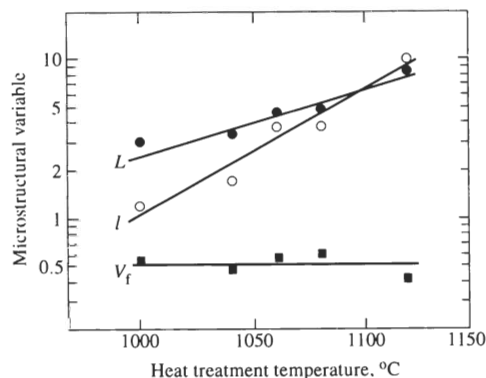
Fig. 2. Plot of mica platelet volume fraction V_f, length l and aspect ratio L of mica platelets in glass-ceramics as function of heat treatment temperature (fixed treatment time 4 h).

2.2. Hertzian test

Hertzian contact damage tests have been well documented for several brittle ceramics [5–10], including a variant of the mica-containing glass-ceramic material system described above [8, 26]. The test itself is simple, involving normal loading of a hard spherical indenter onto a polished flat specimen surface. For the indenter, we use a tungsten carbide sphere of radius $r = 3.18$ mm. Cyclic fatigue tests can be run by repeat loading the sphere.

A bonded-interface configuration, in which two epoxy-bonded half-blocks are indented symmetrically across the interface trace on the top surface and then separated, is used to examine the subsurface damage [7, 8]. Figure 3 includes optical micrographs showing half-surface and section views of a single-cycle indentation made in glass-ceramic heat-treated at 1120°C, at load $P = 2000$ N. In the half-surface view, Fig. 3(a), incipient ring cracks are observed at the periphery of a plastic impression. In the section view, Fig. 3(b), we see no indication of subsurface
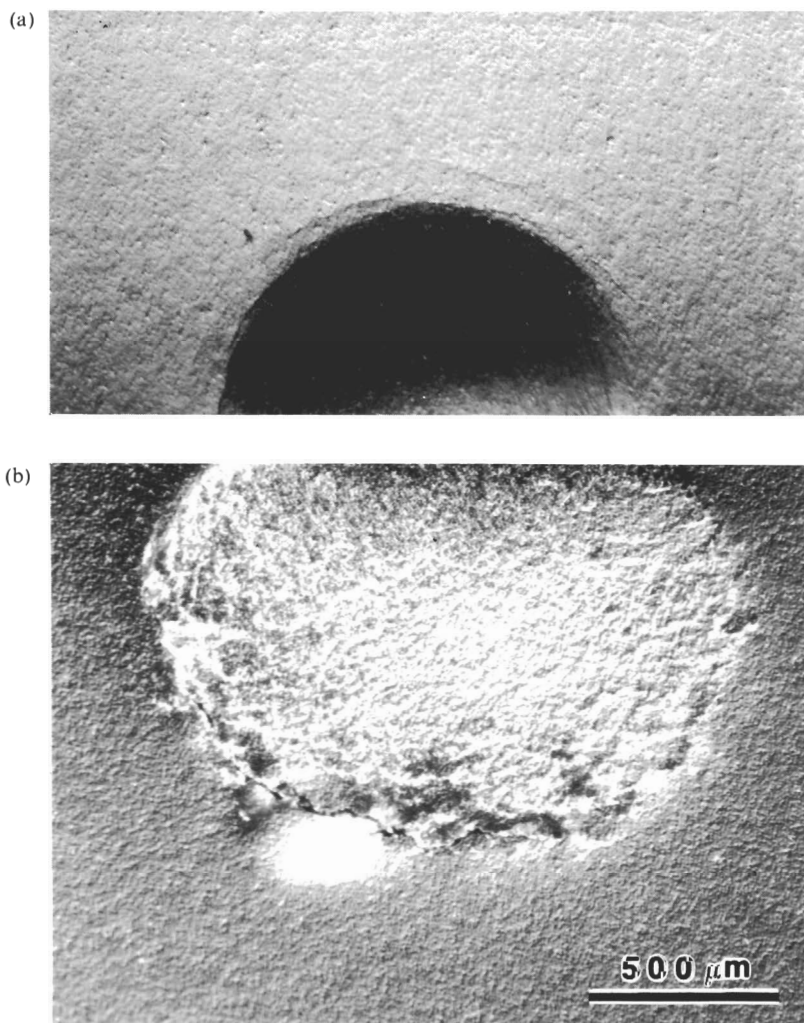

Fig. 3. Optical micrograph (Normarski illumination) of spherical indentation at load $P = 2000$ N (pressure $p_0 = 2.55$ GPa), in glass-ceramic heat-treated at 1060 C. Unetched surfaces from bonded-interface specimen, showing (a) half-surface and (b) section view.
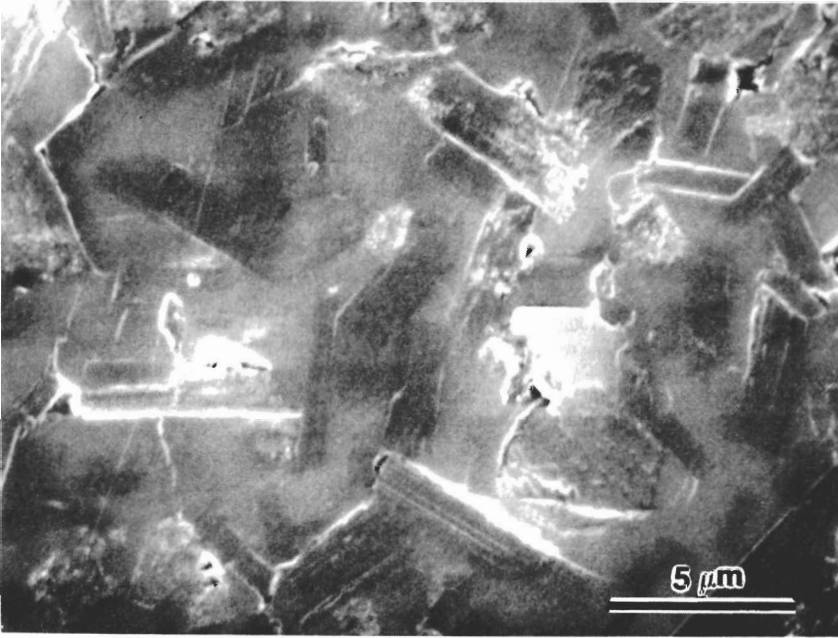
Fig. 4. Scanning electron micrograph from center of section damage region from Fig. 3(b). Microfailures at interphase boundaries are evident.

penetration of the surface cracks into the full cone geometry: the ring cracks appear to have been arrested by deflection away from the tensile stress trajectories [16], along the weak interfaces [24]. Macroscopically, the subsurface damage resembles the plastic zones seen in metals [19]. The damage in Fig. 3(b) appears to be suppressed immediately below the contact zone in the same way, although not to the same degree, as previously reported in a coarser variant of our mica-containing glass-ceramic [8].

Figure 4 is a higher magnification scanning electron micrograph from the central damage region of Fig. 3(b). Microfailures by interfacial breakdown are seen at the interphase boundaries. Such microfailures have been observed even more compellingly in previous studies on other materials; in cyclic loading especially the presence of extruded debris at the damage section attests to the strong role of frictional tractions at the closed, sliding interfaces [26, 27]. No extensile "wing" microcracks are observed at the sliding fault ends [34–36, 38], as one observes in other materials [5–10], although such cracking may well be anticipated at extreme loading conditions (e.g. in machining [29–31] and high-cycle fatigue [27]).

2.3. Indentation stress–strain curves

In the contact field produced by a spherical indenter the intensity of stress is governed by the indentation pressure, $p_0 = P/\pi a^2$, and the strain by the ratio of contact radius to sphere radius, a/r [11, 12]. A straightforward geometrical similarity argument can be used to show that the stress–strain function $p_0(a/r)$ must be a unique function for a given deformable material, regardless of the nature of deformation and

independent of sphere size [11]. Accordingly, a plot of p_0 against a/r, determined from measurements of P and a for a series of indentations at each indentation radius [15], produces a universal indentation stress–strain curve for each material.
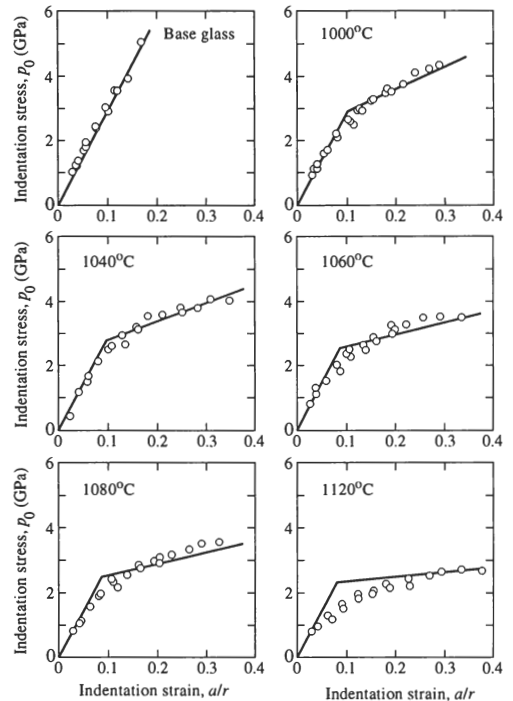

Fig. 5. Indentation stress–strain curves for base glass and glass-ceramics heat-treated at specified temperatures for 4 h. Data from experiments (Section 2), line fits from theoretical analysis (Section 4).

Indentation stress–strain $p_0(a/r)$ data are plotted in Fig. 5 for each of the glass-ceramic heat treatments, and for the base glass. Each data point represents an individual indentation. Solid-line fits through these data are made according to the ensuing theoretical model (Section 3), using a parametric adjustment procedure (Section 4). Note that the nonlinear deviations for the glass-ceramics relative to the base glass become more pronounced, indicating increased plasticity, with increasing heat treatment time.

3. MODEL FOR INDENTATION STRESS–STRAIN CURVE WITH SPHERICAL INDENTERS

In this section we construct a model for Hertzian contact plasticity in ceramics with a high density of discrete weak interfaces. Previous models [24, 25] have focussed on a generic two-step deformation–fracture element, a closed shear fault with extensile cracks at its ends [34–36, 38], embedded in the subcontact compression zone. No direct attention has been given in these previous models to the integrated effect of multiple fault sources on the stress–strain response. Here we are concerned explicitly with the $p_0(a/r)$ function for "underdeveloped" fault systems, notably platelet structures, in which extensile cracks are not yet an essential component of the damage.

Before analyzing the *plastic* contact with spherical indenters, let us consider the perfectly *elastic* Hertzian field as a reference state. Such a field prevails below the shear fault activation stress for deformable ceramics, and is therefore independent of the nature of any ensuing shear fault activity. The well documented Hertzian relation between the indentation stress p_0 and indentation strain a/r is linear proportional:

$$p_0 = (3E/4\pi k)a/r \qquad (1)$$

where E is Young's modulus of the composite specimen material and k is a dimensionless coefficient of the indenter/specimen material system [8, 12, 39]. Because all the parameters in equation (1) are usually specifiable *a priori* for a given indenter/specimen material system, the function $p_0(a/r)$ is predetermined.

3.1. Basic shear fault micromechanics

Now consider the plastic component of the contact field with spherical indenters. In a fully plastic field, the net deformation is the integrated effect of all shear
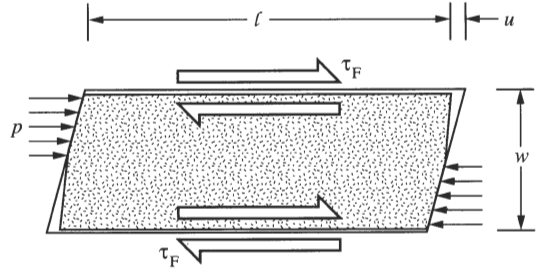
---

†For sliding to occur, the condition $\tau_F \geqslant 0$ must be satisfied in equation (2). It is also implicit that $\sigma_N \leqslant 0$, for otherwise the μ-containing term in equation (2) would disappear. Finally, it is implicit that equation (2) applies only to forward sliding at the fault interface—in backward sliding (as may occur in some unloading half-cycles at very high contact loads) the signs of the two internal friction terms in equation (2) will reverse.

Fig. 6. Deformation of platelet of length l and thickness w within matrix, by sliding at upper and lower interfaces under action of net shear stress τ_F. Sliding is constrained within elastic matrix, by resistive pressures p at ends.

faults within the active zone. In the limit of high volume fractions of particles with large weak interfacial areas, the elastic contribution to the strain may be considered negligibly small.

Our analysis takes as its central deformable element a closed shear fault located at a rectangular platelet/matrix interphase boundary, with frictional tractions at the sliding interface, as in Fig. 6 [25]. Characteristic microstructural dimensions of the platelet are length l and thickness w, corresponding to an aspect ratio $L = l/w$. Constrained slippage occurs at the weak interphase boundaries, the "fault planes". Each individual fault plane is subject to a net shear stress τ_F, consisting of the resolved component from an externally applied field minus terms from internal frictional resistance to sliding [2, 34, 36]. This net shear stress is a function of slip displacement u:

$$\tau_F = |\tau_S - \tau_C| - \mu|\sigma_N| = \kappa u \qquad (2)$$

where τ_S and σ_N are resolved shear and normal compression stresses from the applied field acting on the sliding interface, μ is the coefficient of sliding friction and τ_C the "cohesion" (or "adhesion") strength of the same interface, and κ is an elastic constraint term from the matrix [24].† If residual mismatch stresses σ_R were also to be present at the interphase boundaries, σ_N would simply be replaced by $\sigma_N + \sigma_R$ [25].

The coefficient κ arises from pressures p exerted by the matrix on the constrained half-ends of the deforming platelet and contains essential information on the microstructure. For simplicity, we represent the upper and lower halves of the platelet in Fig. 6 as left- and right-acting cylindrical punches of characteristic radius b, and the confining matrix at each end as load-bearing elastic half-planes. The generic contact relation for such a punch configuration is [39]

$$p = \lambda Eu/b \qquad (3)$$

with λ a geometric coefficient dependent on conditions at the contact interface; e.g. $\lambda = 2/\pi(1 - \nu^2)$
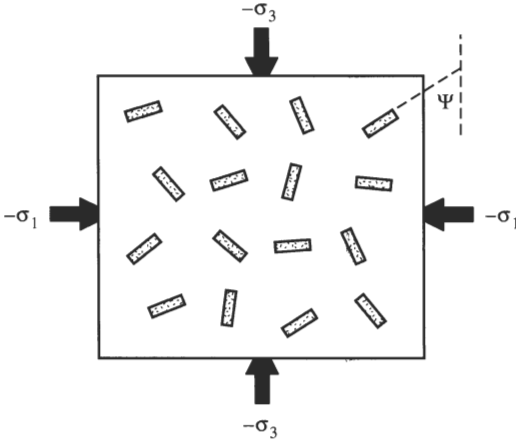
Fig. 7. Volume element in contact stress field, subject to principal compression stresses $-\sigma_3$ and $-\sigma_1$. Element contains distribution of discrete platelets at orientation Ψ to σ_3 axis.

$= 0.55$ at constant u and $\lambda = 3\pi/16(1 - v^2) = 0.68$ at constant p (Poisson's ratio $v = 0.26$) [39]. The characteristic radius b is expressible in terms of the platelet dimensions by defining an equivalent contact area

$$\pi b^2 = lw/2. \qquad (4)$$

The mean contact pressure is also relatable to the frictional shear stress τ_F via the corresponding net shear force $P_F = \tau_F l^2$;

$$p = 2P_F/lw = 2\tau_F l/w. \qquad (5)$$

Combining equations (3)–(5) allows us to determine the constraint coefficient in equation (2):

$$\kappa = (\pi/2)^{1/2} \lambda E w^{1/2}/l^{3/2}. \qquad (6)$$

Now consider a unit of volume within the contact deformation zone containing multiple, noninteracting shear fault elements, as in Fig. 7. Noting that the shear strain for *each* deformed element in Fig. 6 is $e = u/w$, and writing the *net* shear strain over all active elements as $\epsilon_S = eV_f$, we determine a constitutive relation for the contact deformation zone from equations (2) and (6):

$$\tau_F = \epsilon_S E/V_f L^{3/2} \qquad (7)$$

[recalling that $L = l/w$, and approximating $(\pi/2)^{1/2}\lambda$ to unity]. Hence volume fraction V_f and aspect ratio L are important microstructural variables in equation (7), but absolute grain size l is not.

3.2. Stress–strain relation for plastic contact field

In this subsection we seek to derive a $p_0(a/r)$ function for the fully plastic contact with spherical indenter. First, we determine a relation between the frictional shear stress term τ_F and the contact stress p_0. For this we use equation (2), and evaluate τ_S and

σ_N at some "representative" point within the contact deformation zone [24, 25]:

$$\tau_F = [\tfrac{1}{2}(\alpha_3 - \alpha_1) \sin 2\Psi]p_0 - \tau_C$$
$$- \mu[\tfrac{1}{2}(\alpha_3 + \alpha_1) - \tfrac{1}{2}(\alpha_3 - \alpha_1) \cos 2\Psi]p_0 \qquad (8)$$

with $\alpha_1 = -\sigma_1/p_0$ and $\alpha_3 = -\sigma_3/p_0$ positive coefficients, Ψ the angle between the fault plane and σ_3 axis, Fig. 7. In reality, the α terms and Ψ will vary spatially from fault to fault, so strictly a stochastic treatment is in order. However, in the interest of simplicity we shall assume uniform, "averaged" values for these parameters within the contact deformation zone.

Next, we relate the shear strain term ϵ_S to the contact strain a/r. Here we make use of the principle of geometrical similarity, and assert that the strain at any point within the deformation zone is determined uniquely by geometrical considerations, independent of absolute scale of the contact. Accordingly, we may write a simple scaling law [11]

$$\epsilon_S = \beta_S a/r \qquad (9)$$

with β_S a coefficient to be calibrated.

We may now insert (8) and (9) into (7) and solve for $p_0(a/r)$. We obtain the following linear function:

$$p_0 = 2[(\beta_S E/V_f L^{3/2})a/r + \tau_C]/$$
$$\{(\alpha_3 - \alpha_1) \sin 2\Psi - \mu[(\alpha_3 + \alpha_1)$$
$$- (\alpha_3 - \alpha_1) \cos 2\Psi]\}. \qquad (10)$$

Note the dependence on microstructural variables: volume fraction V_f and aspect ratio L, friction parameters τ_C and μ. Again, if residual stresses σ_R were also to be present, τ_C in equation (10) would simply be replaced by $\tau_C - \mu\sigma_R$.

Equation (10) is expected to fit the indentation stress–strain data in the fully plastic region. From such a fit we should be able to calibrate the governing parameters for any given material system.

4. ANALYSIS OF INDENTATION DATA FOR GLASS-CERAMICS

4.1. Parametric fits

We illustrate the theoretical model in Section 3 by plotting equations (1) and (10) as line asymptotes to the glass-ceramic data in Fig. 5. In the elastic region, the lines are preset by inserting $E = 70$ GPs (Section 2.1) and $k = 0.59$ (tungsten carbide on glass-ceramic) [8] in equation (1) for all materials in the series.

In the plastic region, the linear plots are fitted to the data at high strains in accordance with equation (10). Since the linear plots are interrelated via the microstructural variables in equation (10), it is necessary to specify just two independent quantities for the entire set of five glass-ceramics. Accordingly, we fix universal intercept and slope quantities,

$$I = 2\tau_C / \{(\alpha_3 - \alpha_1)\sin 2\Psi - \mu[(\alpha_3 + \alpha_1)$$
$$- (\alpha_3 - \alpha_1)\cos 2\Psi]\} = 2.20 \text{ GPa}$$

$$SV_f L^{3/2} = 2\beta_S E / \{(\alpha_3 - \alpha_1)\sin 2\Psi$$
$$- \mu[(\alpha_3 + \alpha_1)(\alpha_3 - \alpha_1)\cos 2\Psi]\}$$
$$= 24.7 \text{ GPa},$$

and hold volume fraction V_f and friction τ_C constant but allow aspect ratio L to vary in accordance with experimental measurement (Section 2) to obtain the material-to-material variation in Fig. 5.

Thus the model is able to account for the data trends with change in the microstructure, in this specific case in the aspect ratio. It is of corollary interest to evaluate the six individual parameters contained in the intercept and slope quantities I and S in the plastic region, viz. Ψ, α_1 and α_3, β_S, μ and τ_C. Clearly, any such evaluation requires independent information on four of these parameters. Appropriate estimates may be obtained from stress field considerations:

(i) In the interest of a conservative analysis, we assume the most favorable platelet orientation for slip within the contact field, i.e. $\Psi = 45°$ (Fig. 7).

(ii) We use the Hertzian elastic field (at Poisson's ratio 0.26) to obtain estimates of the reduced stress parameters $\alpha_1 = -\sigma_1/p_0$ and $\alpha_3 = -\sigma_3/p_0$ [24]. Again in the interest of a conservative analysis, we evaluate these parameters at the location of maximum shear stress, i.e. at a depth $0.5a$ below the contact center. The principal normal stresses at this point correspond to $\alpha_1 = 0.25$ and $\alpha_3 = 0.74$, the principal shear stress to $\frac{1}{2}(\alpha_3 - \alpha_1) = 0.48$.

(iii) In principle, the friction parameter μ may be estimated from the shape of the subsurface damage zone, specifically from the appearance of a null region immediately below the contact surface where the compressive stresses are so high as to suppress interfacial sliding at the shear faults [8]. Such a region is difficult

to discern in Fig. 3(b), implying that μ must be small for our glass-ceramic. As a first approximation, we take $\mu = 0$.

With these estimates, for $V_f = 0.70 = \text{constant}$ (Section 2), we evaluate $\beta_S = 0.087$ and $\tau_C = 540$ MPa from the data fits for our glass-ceramic system.

We emphasize that the above parameter evaluations are first-order approximations only, and no strong physical significance is therefore meant to be attached to the numbers.

4.2. Determination of intrinsic stress–strain curves

We may use our calibration to determine the intrinsic stress–strain response that would obtain in a uniform compression stress test if it were possible to suppress macroscopic fracture. It is simply a matter of rescaling the axes in the indentation stress–strain diagram. The "constraint factor" for scaling the compression stress axis is simply α_3 in $-\sigma_3 = \alpha_3 p_0$. The "representative strain factor" for scaling the compression strain axis is $\beta = 0.20$ in $\epsilon = \beta a/r$ [11] [cf. β_S in equation (9)].

To illustrate, we generate compression stress–strain functions in Fig. 8 for one of our glass-ceramics, with aspect ratio $L = 4.8 \,\mu$m. We do this by scaling p_0 and a/r in equation (10) as above, for appropriate values of $\sigma_1/\sigma_3 = \alpha_1/\alpha_3$: uniaxial compression (i.e. $-\sigma_1 = 0$), $\alpha_1/\alpha_3 = 0$; confining pressure, $\alpha_1/\alpha_3 = 0.25$, 0.5 and 0.7; "confining" tension, $\alpha_1/\alpha_3 = -1$. Note the enhancement of quasi-ductility with increasing confining pressure (increasing α_1/α_3), consistent with the trends observed in deformation experiments using belt apparatus in rock mechanics [2].

5. DISCUSSION

The Hertzian contact test results described in Section 3 provide fundamental information on the intrinsic properties of otherwise brittle ceramics, information not generally attainable by more conventional testing procedures. Specifically, it enables one to generate (asymptotic) indentation stress–strain curves, such as those shown in Fig. 5 for our glass-ceramic, and thus to quantify any plasticity characteristics. Data of this kind are highly pertinent to structural applications where concentrated stresses are active, e.g. in bearings, in components subject to degradation by impact damage, in contact fatigue and wear, and in machining operations [33]. The generation of quasi-ductility in ceramics offers the prospect of high energy absorption capacity and flaw tolerance, characteristics usually considered to be the exclusive domain of metals [6].

The crux of the present study is the model presented in Sections 3 and 4 describing the high-strain, plasticity regions of the indentation stress–strain curves in Fig. 5. As its central element, the model considers a shear fault at a platelet/matrix interface within the Hertzian contact field, with slippage along
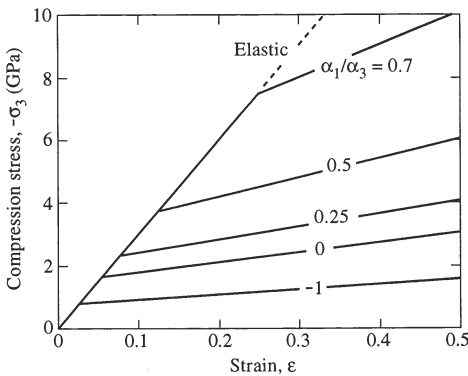

Fig. 8. Intrinsic compression stress–strain curves for glass-ceramic with aspect ratio $L = 4.8$, deduced from calibration of equation (10) using indentation stress–strain data in Fig. 5. Lines for $\alpha_1/\alpha_3 = \sigma_1/\sigma_3 = 0$ (uniaxial compression), $\alpha_1/\alpha_3 = 0.25$, 0.5, 0.7 (compression with confining pressure), and $\alpha_1/\alpha_3 = -1$ (compression with "confining" tension).

the interface and elastic constraint from the embedding matrix at its ends. Starting from a constitutive law for a single fault, a macroscopic stress–strain response is derived by summation over all such faults within the plastic zone. Our description retains the conventional basis of plasticity theory, in that the shear-fault deformation elements are discrete and shear-activated; however, these elements differ fundamentally from the mobile dislocations responsible for classical ductility in metals. An essential ingredient of the description is the existence of resistive frictional tractions at the sliding interfaces, incorporating provision for interfacial attrition and thus for fatigue in cyclic loading [5, 25–27].

A major advantage of the microscopically-based formulation presented here over the more traditional descriptions of indentation plasticity is its emphasis on microstructural variables in equation (10). Interfacial weakness, quantified by low values of μ and τ_C, is the key to a plastic response. For a given material system, the ensuing plasticity is enhanced by large volume fraction V_f and aspect ratio L; however, grain size l is not a direct factor. This independence of grain size in the damage mechanics runs counter to common experience in those materials where extensile "wing" fractures accompanies the shear faults [34–36, 38]; in those cases crack initiation thresholds in microstructural scale are manifest [7, 24].

Whereas our theoretical approach in Section 3 is generic in that it contains the essential ingredients for describing contact plasticity in any ordinarily brittle material with constrained weak interfaces, the indentation stress–strain function in equation (10) relates very specifically to platelet configurations. Also, we have taken the response beyond the elastic limit to be fully plastic in Fig. 5, even though the elastic component is not at all insignificant in the intermediate range of strains (0.1–0.2). Moreover, we have neglected interactions between neighbouring shear faults and ignored the effect of these interactions on the Hertzian elastic field, limiting the plastic stress–strain curve to a linear, monotonically increasing function of strain. In reality, interaction effects can be profound, especially if wing microfractures generate and coalesce at high strains [36], increasing the local compliance in the damage zone [2]. Such interactions can lead to substantial nonlinearities, and even bendover through a maximum ("strain softening"), in the stress–strain curve [2, 3]. In such cases the use of more traditional continuum contact field solutions, e.g. expanding cavity model [39, 40] but modified to include work hardening, might be advocated. On the other hand, such solutions would necessarily circumvent the micromechanical description embodied in Fig. 6, essentially replacing the shear stress parameters by a macroscopic "yield stress", thus precluding the incorporation of basic microstructural variables. Finally, we have ignored stochastical variations in the orientation- and space-sensitive Ψ and α terms in equation (10) within the highly inhomogeneous contact field. These limitations in the modelling, together with the simplifications in the geometrical description in Fig. 6 and the approximations in the parameter calibrations in Section 4.1, suggest that the analysis should not be used to predict more than broad trends in stress–strain responses.

REFERENCES

1. B. R. Lawn, *Fracture of Brittle Solids*, 2nd edn, Cambridge Univ. Press, Cambridge (1993).
2. J. C. Jaeger and N. G. W. Cook, *Fundamentals of Rock Mechanics*, Chapman & Hall, London (1971).
3. S. P. Shah, *NATO Advanced Science Institute Series*, Kluwer Academic, Dordrecht (1990).
4. M. S. Paterson, *Experimental Rock Deformation—The Brittle Field*, Springer, Berlin (1978).
5. F. Guiberteau, N. P. Padture, H. Cai and B. R. Lawn, *Phil. Mag. A* **68**, 1003 (1993).
6. B. R. Lawn, N. P. Padture, H. Cai and F. Guiberteau, *Science* **263**, 1114 (1994).
7. F. Guiberteau, N. P. Padture and B. R. Lawn, *J. Am. Ceram. Soc.* **77**, 1825 (1994).
8. H. Cai, M. A. Stevens Kalceff and B. R. Lawn, *J. Mater. Res.* **9**, 762 (1994).
9. N. P. Padture and B. R. Lawn, *J. Am. Ceram. Soc.* **77**, 2518 (1994).
10. H. H. K. Xu, L. Wei, N. P. Padture, B. R. Lawn and R. L. Yeckley, *J. Mater. Sci.* **30**, 869 (1995).
11. D. Tabor, *Hardness of Metals*, Clarendon, Oxford (1951).
12. M. V. Swain and B. R. Lawn, *Physica status solidi* **35**, 909 (1969).
13. M. V. Swain and J. T. Hagan, *J. Phys. D: Appl. Phys.* **9**, 2201 (1976).
14. H. Hertz, *Hertz's Miscellaneous Paper*, Chaps 5 and 6. Macmillan, London (1896).
15. F. C. Roesler, *Proc. Phys. Soc. Lond.* **B69**, 981 (1956).
16. F. C. Frank and B. R. Lawn, *Proc. R. Soc. Lond.* **A299**, 291 (1967).
17. T. R. Wilshaw, *J. Phys. D: Appl. Phys.* **4**, 1567 (1971).
18. B. R. Lawn and T. R. Wilshaw, *J. Mater. Sci.* **10**, 1049 (1975).
19. T. O. Mulhearn, *J. Mech. Phys. Solids* **7**, 85 (1959).
20. R. Steinbrech, R. Knehans and W. Schaarwächter, *J. Mater. Sci.* **18**, 265 (1983).
21. P. L. Swanson, C. J. Fairbanks, B. R. Lawn, Y.-W. Mai and B. J. Hockey, *J. Am. Ceram. Soc.* **70**, 279 (1987).
22. P. L. Swanson, *Fractography of Glasses and Ceramics* (edited by J. Varner and V. D. Frechette), Vol. 22, p. 135. Am. Ceram. Soc., Columbus, Ohio (1988).
23. S. J. Bennison, J. Rödel, S. Lathabai, P. Chantikul and B. R. Lawn, *Toughening Mechanisms in Quasi-Brittle Materials* (edited by S. P. Shah), p. 209. Kluwer Academic, Dordrecht (1991).
24. B. R. Lawn, N. P. Padture, F. Guiberteau and H. Cai, *Acta metall. mater.* **42**, 1683 (1994).
25. N. P. Padture and B. R. Lawn, *Acta metall. mater.* **43**, 1609 (1995).
26. H. Cai, M. A. S. Kalceff, B. M. Hooks, B. R. Lawn and K. Chyung, *J. Mater. Res.* **9**, 2654 (1994).
27. N. P. Padture and B. R. Lawn, *J. Am. Ceram. Soc.* **78**, 1431 (1995).
28. R. N. Katz and J. G. Hannoosh, *Int. J. High Technol. Ceram.* **1**, 69 (1985).

29. G. H. Beall, *Advances in Nucleation and Crystallization in Glasses* (edited by L. L. Hench and S. W. Freiman), p. 251. Am. Ceram. Soc., Columbus, Ohio (1972).
30. C. K. Chyung, G. H. Beall and D. G. Grossman, *Electron Microscopy and Structure of Materials* (edited by G. Thomas, R. M. Fulrath and R. M. Fisher), p. 1167. Univ. of California Press, Berkeley, Calif. (1972).
31. K. Chyung, *Fracture Mechanics of Ceramics* (edited by R. C. Bradt, D. P. H. Hasselman and F. F. Lange), Vol. 2, p. 495. Plenum Press, New York (1974).
32. C. J. Fairbanks, B. R. Lawn, R. F. Cook and Y. W. Mai, *Fracture Mechanics of Ceramics* (edited by R. C. Bradt, A. G. Evans, D. P. H. Hasselman and F. F. Lange), Vol. 8, p. 23. Plenum Press, New York (1986).
33. N. P. Padture, C. J. Evans, H. H. K. Xu and B. R. Lawn, *J. Am. Ceram. Soc.* **78,** 215 (1995).
34. H. Horii and S. Nemat-Nasser, *J. Geophys. Res.* **90,** 3105 (1985).
35. H. Horii and S. Nemat-Nasser, *Phil. Trans. R. Soc. Lond.* **319,** 337 (1986).
36. M. F. Ashby and S. D. Hallam, *Acta metall.* **34,** 497 (1986).
37. D. G. Grossman, *Proceedings of the International Symposium on Computer Restorations* (edited by W. H. Mörmann), p. 103. Quintessence, Chicago, Il (1991).
38. J. M. Kemeny and N. G. W. Cook, *Toughening Mechanisms in Quasi-Brittle Materials* (edited by S. P. Shah), p. 287. Kluwer Academic, Dordrecht (1991).
39. K. L. Johnson, *Contact Mechanics*, Cambridge Univ. Press, London (1985).
40. R. Hill, *The Mathematical Theory of Plasticity*, Oxford Univ. Press, London (1950).